Journal of Instrumentation

PAPER • OPEN ACCESS

Study of the internal quantum efficiency of FBK sensors with optimized entrance windows

To cite this article: M. Carulla *et al* 2023 *JINST* **18** C01073

View the article online for updates and enhancements.

You may also like

- Triple-differential cross sections for the ionization of thymine by electrons and positrons
C Dal Cappello, I Charpentier, S Houamer et al.

- Theoretical study of (e,2e) triple differential cross section of $1b_{3g}$ orbital of ethylene by vibrational multi-center distorted-wave method
Zhenpeng Wang, , Maomao Gong et al.

- Swelling as a stabilizing mechanism in irradiated thin films: III. Effect on critical angle in a composite model
Tyler Evans and Scott Norris

This content was downloaded from IP address 213.215.189.91 on 22/02/2024 at 16:44

Jinst

PUBLISHED BY IOP PUBLISHING FOR SISSA MEDIALAB

RECEIVED: October 3, 2022
ACCEPTED: December 21, 2022
PUBLISHED: January 31, 2023

23ND INTERNATIONAL WORKSHOP ON RADIATION IMAGING DETECTORS
26–30 JUNE 2022
RIVA DEL GARDA, ITALY

Study of the internal quantum efficiency of FBK sensors with optimized entrance windows

M. Carulla,[a,*] M. Centis Vignali,[b] R. Barten,[a] F. Baruffaldi,[a] A. Bergamaschi,[a] G. Borghi,[b] M. Boscardin,[b] M. Brückner,[a] R. Dinapoli,[a] S. Ebner,[a] F. Ficorella,[b] E. Fröjd,[a] D. Greiffenberg,[a] O. Hammad Ali,[b] S. Hasanaj,[a] J. Heymes,[a] V. Hinger,[a] T. King,[a] P. Kozlowski,[a] C. Lopez Cuenca,[a] D. Mezza,[a] K. Moustakas,[a] A. Mozzanica,[a] G. Paternoster,[b] S. Ronchin,[b] C. Ruder,[a] B. Schmitt,[a] D. Thattil[a] and J. Zhang[a]

[a] *PSD Detector Group, Paul Scherrer Insitut, Forschungsstrasse 111, 5232 Villigen PSI, Switzerland*

[b] *Fondazione Bruno Kessler, Via Sommarive 18, 38126 Povo TN, Italy*

E-mail: maria.carulla@psi.ch

ABSTRACT: Single-photon detection of X-rays in the energy range of 250 eV to 1 keV is difficult for hybrid detectors because of the low quantum efficiency and low signal-to-noise ratio. The low quantum efficiency is caused by the absorption of soft X-rays in the entrance window of the silicon sensors. The entrance window consists of an insensitive layer on the surface and a highly doped layer, which is typically from a few hundred nanometers to a couple of micrometers thick and is comparable to the absorption depth of soft X-ray photons (e.g. the attenuation length of 250 eV X-ray photons is ∼100 nm in silicon). The low signal-to-noise ratio is mainly caused by the small signal amplitude (e.g. ca. 70 electrons for 250 eV X-ray photons in silicon) with respect to the electronic noise. To improve the quantum efficiency, the entrance window must be optimized by minimizing the absorption of soft X-rays in the insensitive layer, and reducing charge recombination at the Si-SiO_2 interface and in the highly doped region. Low gain avalanche diodes (LGADs) with a multiplication factor between 5 and 10 increase the signal amplitude and therefore improve the signal-to-noise ratio for soft X-rays, enabling single-photon detection down to 250 eV. Combining LGAD technology with an optimized entrance window technology can thus allow hybrid detectors to become a useful tool also for soft X-ray detection. In this work we present the optimization of the entrance window by studying the internal quantum efficiency of eight different process technology variations. The sensors are characterized using light emitting diodes with a

2023 JINST 18 C01073

*Corresponding author.

© 2023 The Author(s). Published by IOP Publishing Ltd on behalf of Sissa Medialab. Original content from this work may be used under the terms of the Creative Commons Attribution 4.0 licence. Any further distribution of this work must maintain attribution to the author(s) and the title of the work, journal citation and DOI.

https://doi.org/10.1088/1748-0221/18/01/C01073

wavelength of 405 nm. At this wavelength, the light has an absorption depth of 125 nm, equivalent to that of 276 eV X-rays. The best variation achieves an internal quantum efficiency of 0.992 for 405 nm UV light. Based on this study, further optimization of the quantum efficiency for soft X-rays detection is planned.

Keywords: X-ray detectors; Solid state detectors; Radiation and optical windows

2023 JINST 18 C01073

Contents

1 Introduction **1**

2 Study of thin entrance window sensors **1**

2.1 Process variations of the TEW R & D batch 2

2.2 Internal quantum efficiency 3

2.2.1 Measurement set-up and sensor design 3

2.2.2 Results 4

3 Conclusions **8**

1 Introduction

Single-photon detection with high efficiency in the soft X-ray energy range (between 250 eV and 1 keV) with position sensitive hybrid X-ray detectors is challenging due to the low quantum efficiency (QE) and the low signal-to-noise ratio (SNR). The low QE in this photon energy range is due to the short attenuation length of soft X-rays. Standard silicon sensors used for hard X-rays or minimum ionizing particles detection have a thick entrance window (EW) with an aluminum layer thickness between hundreds of nanometers and some micrometers as well as an approximately 1 µm deep highly doped n^{+} region. Thus, in the case of standard silicon sensors, the soft X-ray photons are absorbed in the EW resulting in a low QE. The measured QE of a standard silicon sensor for 800 eV X-ray photons is less than 50% as presented in ref. [1]. Therefore, an optimization of the EW technology is required to reduce the recombination in the silicon and at the silicon surface, at the same time that the transmittance in the surface layer is increased. Although in the present study we focus in the optimization of the EW for soft X-rays, the improvement of the QE is not enough to obtain single-photon detection for soft X-rays with energies lower than 800 eV using the JUNGFRAU 1.1 readout ref. [2]. Therefore the SNR should be increased. The use of the new entrance window technology together with LGADs technology allows the single-photon detection of X-rays with energies lower than 800 eV, as already demonstrated by J. Zhang et al. ref. [1].

2 Study of thin entrance window sensors

Since 2019 the PSI detector group has been collaborating with Fondazione Bruno Kessler (FBK) to develop a backside thin entrance window (TEW) technology suited for soft X-rays. In the framework of this collaboration, FBK produced an R & D batch with 9 different process variations in order to optimize the n^{+} implant, the silicon surface and the thickness of the surface layer. Table 1 shows the process variations of the R & D batch.

2023 JINST 18 C01073

Table 1. Main specifications of different process variations for the TEW R & D batch.

Wafer #	Si orientation	n^+ impurity	Dose	Annealing temperature	Surface layer
1–2	⟨111⟩	As	High	High	Aluminum
3–4, 7–8	⟨111⟩	As	High	High	SiO_2 and Si_3N_4
5–6	⟨111⟩	As	High	Low	SiO_2 and Si_3N_4
9–10	⟨111⟩	As	Low	Low	SiO_2 and Si_3N_4
11–12	⟨100⟩	As	High	High	SiO_2 and Si_3N_4
13–14	⟨111⟩	As	High	High	Thin SiO_2 and Si_3N_4
15–16	⟨111⟩	P	Low	Low	SiO_2 and Si_3N_4
17–18	⟨111⟩	P	High	High	SiO_2 and Si_3N_4
19–20	⟨100⟩	P	High	High	SiO_2 and Si_3N_4

2.1 Process variations of the TEW R & D batch

The sensors were fabricated on n-type silicon wafers with average resistivity equal to 7.5 kΩ · cm for wafers with crystal orientation ⟨100⟩ and 13.5 kΩ · cm for wafers with crystal orientation ⟨111⟩. The wafer thickness is 450 µm for the ⟨100⟩ wafers and 300 µm for the ⟨111⟩ ones. Thus, the diodes have to be biased at 92 V for the ⟨100⟩ wafers and 23 V for the ⟨111⟩ wafers in order to be fully depleted. The pn-junction of the sensor is placed on the pixel side, with the pixels being a p-type doped region. The backside of the sensor (the EW) consists of an n-type (n^+) doped region, realized either through arsenic implantation or phosphorus diffusion. The EW region is passivated with a SiO_2 and a Si_3N_4 layer, with a total thickness of a few tens of nanometers. The total thickness of the passivation layers was reduced on two wafers, namely wafer 13 and 14, to explore the feasibility of this procedure. Wafer 1 and 2 have a different passivation consisting of an aluminum layer with a thickness of a few hundred nanometers.

Table 2 shows the average volume leakage current of test structures placed at the periphery of the produced wafers. The ⟨100⟩ wafers show a higher value of leakage than the ⟨111⟩ wafers, this is attributed to the difference in the impurities present in the starting material rather than the crystal orientation. Furthermore, the leakage current for wafers with low annealing temperature is lower than for wafers with high annealing temperature. Gate controlled diodes are also placed in each wafer to measure the surface leakage current and study the surface recombination velocity at the Si-SiO_2 interface on the pixel side. Table 2 presents the surface recombination velocity for the different process variations. The surface recombination velocity was measured on a single gated diode for each process variation. For the ⟨100⟩ wafers, the surface recombination velocity could not be measured as the shape of the current as a function of gate voltage did not allow for an estimation of the surface current of the device. The values of surface recombination velocity for the ⟨100⟩ wafers are expected to be lower than the ones measured for the ⟨111⟩ wafers. Overall, the values of surface recombination are satisfactory for the pixel side of the sensors, and in line with the values obtained for similar fabrication processes. The surface recombination velocities at the Si-SiO_2 interface for the clean oxide without implantation on the EW side of the sensors are expected to be different and present lower values than the pixel side due to the different process used to passivate the EW.

2023 JINST 18 C01073

Table 2. Leakage current and surface recombination velocity on the pixel side of the sensor.

Wafer	Leakage current [μA/cm^3]	Surface recombination velocity (pixel side) [cm/s]
1–2	5.1 ± 0.5	1.799 ± 0.017
3–4, 7–8	4.4 ± 0.3	4.281 ± 0.014
5–6	1.8 ± 0.4	4.191 ± 0.019
9–10	2.5 ± 0.4	5.368 ± 0.014
11–12	9.1 ± 0.6	—
13–14	5.3 ± 0.6	3.148 ± 0.025
15–16	3.2 ± 0.5	5.659 ± 0.016
17–18	3.9 ± 0.6	4.924 ± 0.018
19–20	7.3 ± 0.5	—

2.2 Internal quantum efficiency

The internal quantum efficiency (IQE) of a photo-diode illuminated with visible light is defined as the ratio between the number of collected electron-hole (e-h) pairs and the number of absorbed photons ref. [3], since the quantum yield of silicon is equal to one in the visible range. In comparison, the external quantum efficiency (EQE) or quantum efficiency (QE) is the number of collected e-h pairs divided by the number of incident photons on the photo-diode. Therefore, the QE also takes into account the reflected light, given that the transmittance of 300 μm thick silicon photo-diode is negligible in the visible range.

In this work, we will focus on the IQE measurements of one sensor of each split specified in table 1, namely wafer 5, 7, 9, 11, 13, 15, 17 and 19, using an LED with a wavelength of 405 nm (UV light). Since wafer 1 and 2 are based on a single-side process without patterning of the backside aluminum layer, this split cannot be tested by means of UV light. However, the process has been studied and reported in ref. [2].

2.2.1 Measurement set-up and sensor design

In order to investigate the IQE, we have designed a pixelated test sensor consisting of a 2×5 pixel array. Each pixel is wire-bonded to a readout channel to measure its photocurrent. On the pixel side a collector ring surrounds the pixel array as presented in figure 1(a) to collect the leakage current and photocurrent generated at the periphery. Figure 1(b) shows the backside view of the pixel array, where each row of the array has a defined area opened on the metal layer. The size of the metal opening ranges from 10×10 μm^2 on the last row to 100×100 μm^2 on the first row. Figure 1(c) shows the cross section of the sensor through the row cut, where the opening on the pixels on the first column is without n^+ doping. Therefore, the reduction in the collected charge due to recombination on the n^+ region can be evaluated by comparing the photocurrents of the pixels on the first and second column. From the surface leakage current measurements, we obtained a negligible surface recombination velocity in the SiO_2/Si interface without n^+ doping in the silicon. Thus, the number of e-h pairs generated in the pixel without n^+ doping can be considered equal to the number of photons absorbed and the ratio between the pixel with and without n^+ doping is equal to the IQE of the sensor ref. [4].

2023 JINST 18 C01073

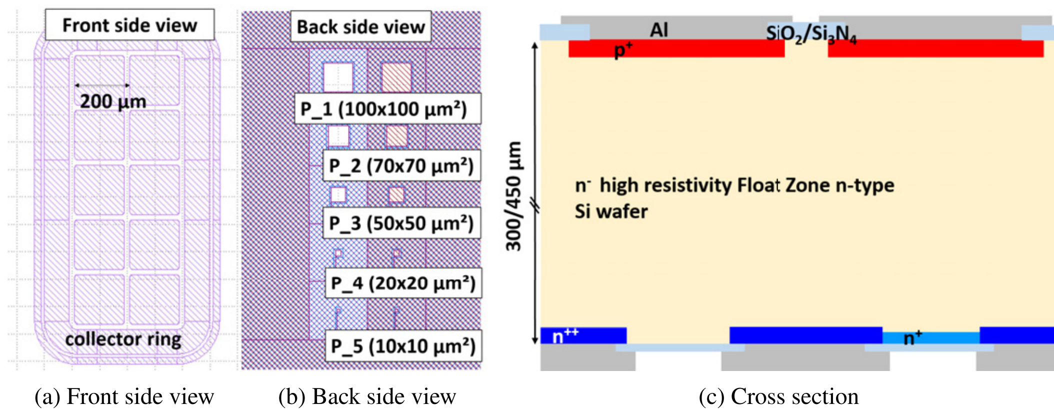

(a) Front side view (b) Back side view (c) Cross section

Figure 1. Front side view (a), back side view (b) and cross section (c) of the pixel array under test.

For this study, the pixelated sensor is glued and bonded to a PCB that is mounted on a stage with a motor on each one of the three axes. A Keithley 2410 is used to reverse bias the sensor. The sensor is illuminated from the backside with a fiber coupled LED from ThorLabs (M405FP1) with 405 nm wavelength and 12 nm FWHM, which is in contact with a cooling plate and is kept at 20 C by a chiller. The currents of pixels with and without n^+ doping are measured simultaneously with a picoammeter Keithley 6487 and a Keithley 6485. Figure 2 depicts an schematic of the setup.

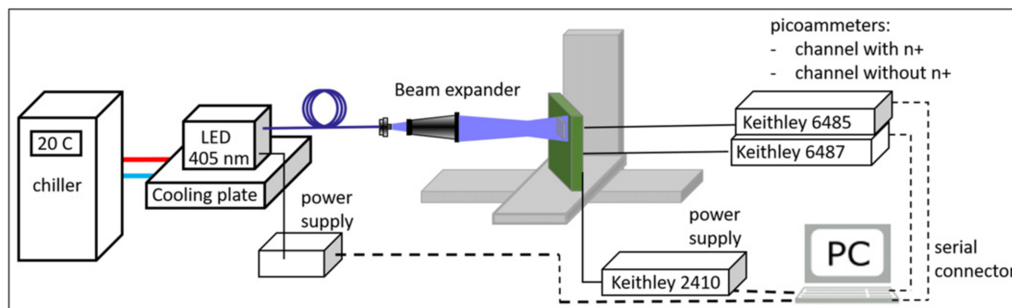

Figure 2. Experimental setup.

2.2.2 Results

Before the photocurrent is measured, the measurement of the leakage current as a function of the reverse bias voltage is performed under dark conditions. Figures 3(a) and (b) show the summary of the leakage current measurements for the pixels with and without n^+ doping, respectively. The area of the opening in these pixels is $100 \times 100\ \mu\text{m}^2$. As shown in figure 3(a) wafers 5 (orange dots), 9 (red dots) and 15 (pink dots), which are annealed at low temperature, have a lower leakage current in comparison to the wafers with high temperature annealing.

2023 JINST 18 C01073

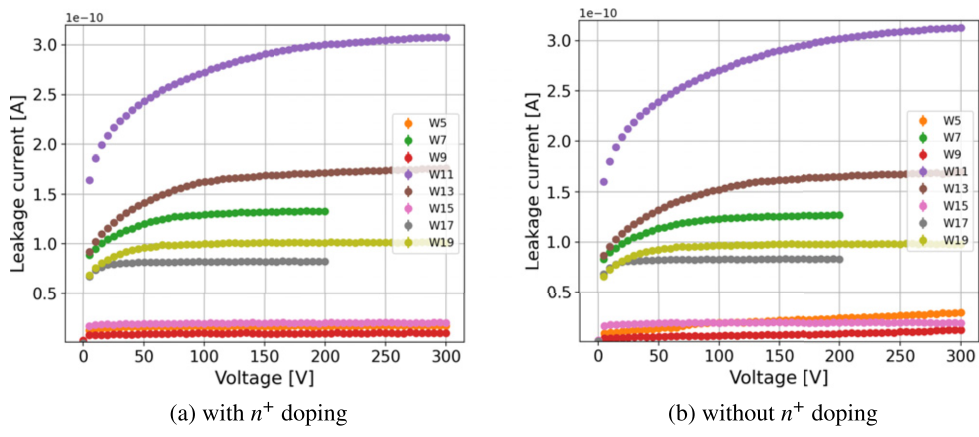

(a) with n^+ doping (b) without n^+ doping

Figure 3. Leakage current measurement for pixels with and without n^+ doping below the opening on the backside for wafers 5, 7, 9, 11, 13, 15, 17 and 19.

In order to uniformly illuminate the pixels with and without n^+ doping, the sensor is moved away from the beam focal point to a position where the beam has a FWHM of approximately 3 mm. Considering the absorption coefficient of aluminum ref. [5], the aluminum suppresses the transmission of 405 nm UV light by 11 orders of magnitude. Therefore, the illuminated area is equal to the area of the opening of the metal layer. Once the beam is unfocused, it is scanned through the metal openings of both pixels and the photocurrent is calculated by subtracting the leakage current to the measurement of the current under illumination. First a rough scan is performed in the X axis to center the beam in the middle position between the pixels center. Afterwards, a fine scan in the Y axis is carried out to find the center position. Finally, a fine scan in the X axis is done. The photocurrent measurement of the scans in the X and Y axis are presented in figures 4(a) and (b), respectively. As it is shown in the X axis scan in figure 4(a), the curves of the pixel with and without n^+ doping are displaced by 200 µm, which is the pixel pitch. The difference between centering the beam at the middle point between pixels and at the center of each pixel is less than 1% for all the cases. Therefore, the beam is centered in the middle point between pixels. Thus, both pixels are measured at the same time.

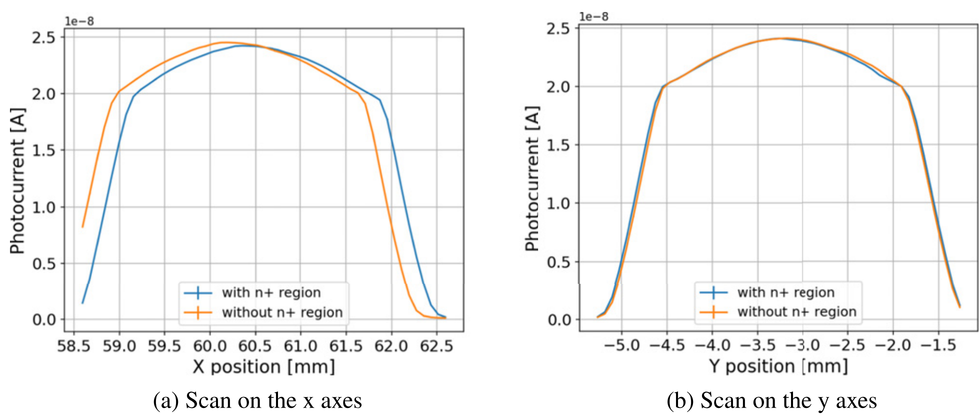

(a) Scan on the x axes (b) Scan on the y axes

Figure 4. Alignment scan through the x axes (a) and y axes (b).

2023 JINST 18 C01073

Once the sensor is aligned, the stability of the IQE measurement is verified by measuring the currents of both pixels for more than 2 hours, as shown in figure 5(a). The data in the figure is for pixels from wafer 11 with a $70 \times 70\ \mu\mathrm{m}^2$ opening. Although there is a clear increase of the photocurrent as a consequence of the thermal drift of the LED, the standard deviation of the IQE over the entire measurement is less than 0.3%. All the photocurrent measurements are performed after 15 minutes of switching on the LED to avoid differences in the LED power due to changes of the refraction index of the fiber ref. [6].

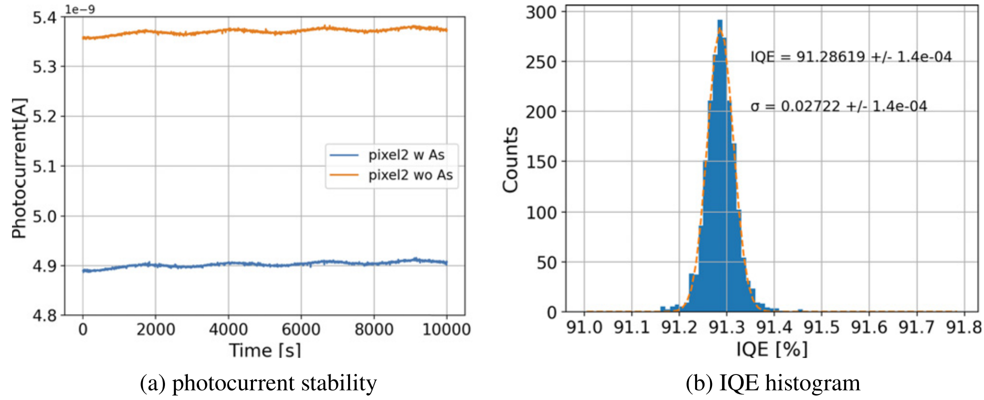

(a) photocurrent stability

(b) IQE histogram

Figure 5. Measurement of the photocurrent as a function of the time for wafer 11 (a) and the corresponding IQE distribution (b).

After the alignment and the stability test are carried out, the photocurrent as a function of the reverse bias voltage is performed for all the pixels of the sensor. The photocurrents as a function of the illuminated area, which is the area of the metal opening, for the sensor biased at 200 V are plotted in figure 6. Figures 6(a) and (b) show the photocurrent for the pixels with and without n^+ doping, respectively. Since the surface recombination velocity depends on the silicon crystal orientation and the thermal process, refs. [7, 8], the photocurrents of the pixels without n^+ doping for wafers with the same thermal process and crystal orientation, namely wafer 5 (orange triangles) and 9 (red triangles) or wafer 7 (green triangles) and 13 (brown squares), should be equal. Therefore the ~1% difference in the photocurrent measurements for these wafers, which is shown in figure 6(b), is attributed to differences in the reflectance or LED power.

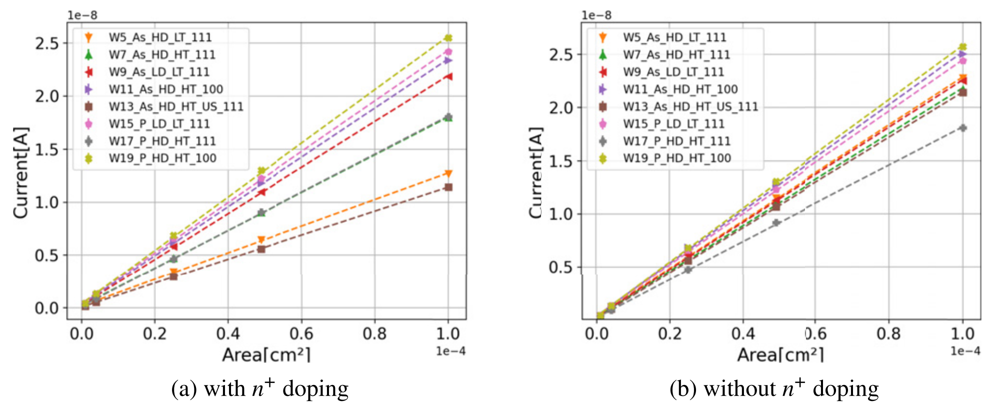

(a) with n^+ doping

(b) without n^+ doping

Figure 6. Photocurrent as a function of the area of the metal opening.

2023 JINST 18 C01073

The IQE as function of reverse bias voltage for the different wafers is summarized in figure 7. The highest IQE is obtained for wafer 15, in which the n^+ doping is done by phosphorus diffusion. All the phosphorus diffused sensors show higher IQE in comparison to arsenic implanted wafers due to a doping profile with a lower peak concentration in comparison to arsenic, although the tail is longer than in the arsenic implant. The lowest IQE is measured for wafer 5 (orange dots) with a high arsenic implantation dose and low thermal annealing. In this case the damage introduced by implantation is not annealed and the IQE is drastically reduced in comparison to wafer 7 (green dots) with a high thermal annealing. On the other hand, wafer 9 (red dots) with a low implant dose and low thermal annealing shows the highest IQE for the arsenic implanted wafers. Curiously, wafer 13 (brown dots) which has the same process as wafer 7 (green dots) but thinner Si_3N_4 and SiO_2 surface layer shows a notable decrease in the IQE that cannot be explained by the differences in the doping profile or surface recombination. In this case, the standard deviation of the Si_3N_4 and SiO_2 thicknesses measurement is 54% and 21% of the nominal values, respectively. This variation on the surface layer thicknesses can give rise to a reflectance difference of 36% from one pixel to another. The measurement of this sensor will be verified with X-rays in order to understand whether the observed decrease is due to reflectance variations or another effect. Another interesting result is the IQE difference between wafer 11 (violet dots) produced on Si $\langle 100 \rangle$ and wafer 7 (green dots) produced on Si $\langle 111 \rangle$. In this case, the difference in the IQE cannot be explained from the doping profile or reflectance variations. Therefore, the higher IQE in Si $\langle 100 \rangle$ than in Si $\langle 111 \rangle$ indicates a lower surface recombination velocity in Si $\langle 100 \rangle$ than in Si $\langle 111 \rangle$.

2023 JINST 18 C01073

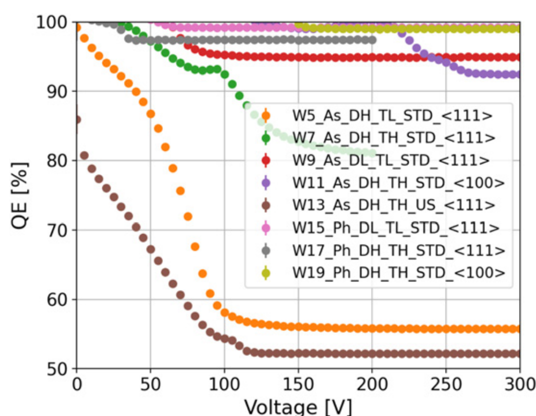

Figure 7. Internal quantum efficiency for the different wafer splits of the R & D batch.

The absorption depth of UV light with a wavelength of 405 nm in silicon is 125 nm. This absorption depth is obtained by interpolating the log-log data tabulated by Green in ref. [9]. Since photons with an energy of 276 eV have an attenuation length of 125 nm ref. [10], the quantum efficiency of 276 eV X-ray photons can be calculated using the Lambert-Beer law and by knowing the insulator thicknesses, which were measured by FBK and are confidential. The expected QE for arsenic implanted and phosphorus diffused wafers for 276 eV X-ray photons are presented in tables 3 and 4, respectively. Sensors with phosphorus diffused EW show in general higher QE in

comparison to arsenic implanted sensors thanks to the high IQE. The calculated QE for the best split is approximately the same as the obtained by backside-illuminated scientific CMOS detectors ref. [11] and approximately a 6% lower QE than the 75% QE obtained using backside illuminated pn-CCD detectors ref. [12].

Table 3. Summary of the IQE measurement (meas.) and QE calculation (cal.) for arsenic implanted sensors.

Wafers	5	7	9	11	13
IQE[%]@405 nm (meas.)	55.75 ± 0.01	81.11 ± 0.02	94.94 ± 0.03	91.44 ± 0.02	52.18 ± 0.01
QE[%]@276 eV (cal.)	37.87 ± 0.01	55.10 ± 0.02	64.49 ± 0.03	67.17 ± 0.02	43.40 ± 0.01

Table 4. Summary of the IQE measurement (meas.) and QE calculation (cal.) for phosphorus diffused sensors.

Wafers	15	17	19
IQE[%]@405 nm (meas.)	99.22 ± 0.03	97.41 ± 0.05	99.06 ± 0.05
QE[%]@276 eV (cal.)	68.62 ± 0.03	70.15 ± 0.02	66.70 ± 0.05

3 Conclusions

This work presents the measurements of the internal quantum efficiency of an R & D batch with optimized entrance windows using an optical setup. This study demonstrates the increase of the IQE from 81.11% on wafers with an arsenic implant up to 99.22% on wafers with phosphorus diffusion. It also points out the improvement of the IQE when sensors are produced on Si ⟨100⟩ wafers instead of Si ⟨111⟩ wafers. As expected, the results show an increase of the IQE when the doping profile peak is reduced. Interestingly, the IQE can be further improved when the dose and the temperature annealing is reduced. We also find out that a low thermal annealing when a high dose is implanted reduces the IQE due to the fact that the annealing of the implant damage is not enough. Based on the study of this batch, we are preparing a new batch to further optimize the dose and temperature annealing for Si ⟨100⟩ wafers and to reduce the Si_3N_4 and SiO_2 thicknesses, which are important for the increase of the QE for soft X-rays. Thus, this improvement in the QE in comparison to standard sensors together with the increase of the SNR using iLGAD technology in the future, make us confident that single-photon detection for 276 eV photons will be possible for hybrid detectors.

Acknowledgments

The authors thank K. Vogelsang from the laboratory for X-ray nanoscience and technologies of PSI for his help dicing the sensors. One of the authors (V. Hinger) has received funding from MSCA PSI-FELLOW-III-3i (EU Grant Agreement No. 884104).

2023 JINST 18 C01073

References

[1] J. Zhang, R. Barten, F. Baruffaldi, A. Bergamaschi, G. Borghi, M. Boscardin et al., *Development of LGAD sensors with a thin entrance window for soft X-ray detection*, 2022 *JINST* **17** C11011.

[2] V. Hinger, A. al Haddad, R. Barten, A. Bergamaschi, M. Brückner, M. Carulla et al., *Advancing the JUNGFRAU detector toward low-energy X-ray applications*, 2022 *JINST* **17** C09027.

[3] A. Ferrero, J. Campos, A. Pons and A. Corrons, *New model for the internal quantum efficiency of photodiodes based on photocurrent analysis*, *Appl. Opt.* **44** (2005) 208.

[4] J. Geist and C.S. Wang, *New calculations of the quantum yield of silicon in the near ultraviolet*, *Phys. Rev. B* **27** (1983) 4841.

[5] L.G. Schulz, *The optical constants of silver, gold, copper, and aluminum. I. The absorption coefficient k*, *J. Opt. Soc. Am.* **44** (1954) 357.

[6] Thorlabs, Fiber-coupled led, 405 nm.

[7] S.C. Baker-Finch and K.R. McIntosh, *The contribution of planes, vertices, and edges to recombination at pyramidally textured surfaces*, *IEEE J. Photovoltaics* **1** (2011) 59.

[8] H. Fukuda, M. Yasuda, T. Iwabuchi, S. Kaneko, T. Ueno and I. Ohdomari, *Process dependence of the SiO_2/Si(100) interface trap density of ultrathin SiO_2 films*, *J. Appl. Phys.* **72** (1992) 1906.

[9] M.A. Green and M.J. Keevers, *Optical properties of intrinsic silicon at 300 K*, *Prog. Photovoltaics* **3** (1995) 189.

[10] J. Hubbel and S. Seltzer, *X-ray mass attenuation coefficients*, NIST Standard Reference Database 126.

[11] K. Desjardins, K. Medjoubi, M. Sacchi, H. Popescu, R. Gaudemer, R. Belkhou et al., *Backside-illuminated scientific CMOS detector for soft X-ray resonant scattering and ptychography*, *J. Synchrotron Radiat.* **27** (2020) 1577.

[12] R. Hartmann, K.-H. Stephan and L. Strüder, *The quantum efficiency of pn-detectors from the near infrared to the soft X-ray region*, *Nucl. Instrum. Meth. A* **439** (2000) 216.

2023 JINST 18 C01073